Unified insights: Relativistic density functional theory for proton resonance, emission, and proton-rich exotic nuclei

Shu-Yuan Zhai, Jian-You Guo [*] and Quan Liu [†]

School of Physics and Optoelectronic Engineering, Anhui University, Hefei 230601, People's Republic of China

We have presented an enhanced relativistic density functional theory that comprehensively addresses proton resonance, emission processes, and proton-rich exotic nuclei. Our theory successfully resolves the long-range Coulomb potential issue by eliminating its singularity within the Dirac equation using the complex momentum representation. When applied to ^{120}Sn, our theory significantly improves alignment with advanced scattering data, surpassing the accuracy of traditional methods, even for exceptionally broad resonances. Additionally, our analysis of proton emissions from ^{37}Sc and ^{39}Sc accurately reproduces experimental Q values and lifetimes. Our model exhibits superior agreement with time-dependent Dirac calculations compared to other methodologies, particularly in capturing nuances of narrow widths. Extending to proton-rich exotic nuclei, such as ^{26}P, we unveil detailed density distributions unconstrained by box size, revealing proton halo characteristics due to weakly bound $2s_{1/2}$ protons. This advancement in our relativistic density functional theory gives hope for reaching a more accurate and comprehensive understanding of nuclear phenomena across proton-rich systems.

I. INTRODUCTION

The exploration of weakly bound and unbound nuclei, distant from the stability line, constitutes a crucial domain in nuclear physics and astrophysics [1,2]. Neutron-rich and proton-rich regions exhibit numerous exotic phenomena, including halo structures, single (double) neutron (proton) emissions, continuous state coupling, and magic number shifts [3,4]. While traditional models like the shell model and (non-) relativistic density functional theories succeed with stable nuclei, their application to exotic nuclei demands consideration of the continuum and resonances within it.

Addressing the continuum, the Gamow shell model excels in describing light exotic nuclei [5,6]. For heavier exotic nuclei, the continuum Hartree-Fock Bogoliubov theory [7–9] and the widely embraced relativistic mean field (RMF) theory [10–16] have been employed. Understanding exotic phenomena necessitates investigating physical resonance states, leading to the integration of various resonance methods, such as analytic continuation of coupling constants (ACCC) [17], stabilization method (SM) [18], complex scaling method (CSM) [19,20], Green's function [21], scattering phase shift [22,23], Jost function [24,25], and complex-scaled Green function [26,27], and others, with RMF.

Recently, the complex momentum representation (CMR) method has gained prominence for its effectiveness in describing resonant states and exotic nuclei. CMR's versatility in handling bound and resonant states in both narrow and broad spectra makes it invaluable for investigating weakly bound and unbound nuclei. In the nonrelativistic context, CMR has been extensively used for both bound [28,29] and resonant states [30–32], forming the basis for the Gamow shell model for weakly bound nuclei [33].

Capitalizing on CMR's advantages, we extended its application to the relativistic framework, resulting in the RMF-CMR theory [34]. This theory enabled comprehensive investigations into exotic properties of spherical and deformed nuclei [35–39]. While previous studies primarily focused on neutron-rich nuclei, attention was directed to proton-rich nuclei, highlighting phenomena like proton halos and emissions. The pivotal role of the long-range Coulomb field in proton-rich nuclei motivated us to address its singularity in the momentum representation. To tackle this issue, we incorporate the Lande subtraction method, which has proven effective in removing singularities in the long-range Coulomb potential within a nonrelativistic framework [40–43]. In this work we utilize the Lande subtraction to tackle the enduring issue of the Coulomb field's long-range behavior within the context of relativistic density functional theory.

This enhanced RMF-CMR theory, applicable to both neutron-rich and proton-rich nuclei, has been instrumental in studying proton resonances, emissions, and exotic properties. It provides insights into the mechanisms governing proton decay and the formation of proton halos in atomic nuclei. Notably, the theory excels in exploring both extraordinarily broad and narrow resonances, overcoming significant challenges. Section II details the theoretical framework, Sec. III discusses numerical aspects and presents results, while Sec. IV offers a comprehensive summary.

II. FORMALISM

In the conventional RMF-CMR theory, both the Coulomb long-range potential and meson-exchange potential are treated

---

*Contact author: jianyou@ahu.edu.cn
†Contact author: Quanliu@ahu.edu.cn

equally, a successful approach for studying neutron-rich exotic nuclei. However, for proton-rich exotic nuclei, addressing the Coulomb field is crucial to eliminate the singularity arising in the Dirac equation. In the following we delve into the theoretical framework.

The Dirac equation from the RMF can be expressed as follows:

$$[\vec{\alpha} \cdot \vec{p} + \beta(M + S) + V]\psi = \varepsilon\psi, \tag{1}$$

where M represents the nucleon mass, $\vec{\alpha}$ and β are the Dirac matrices, and S and V are the scalar and vector potentials, respectively. The vector potential V consists of V_o and V_c. V_o (V_c) represents that contributed by exchange vector mesons (photon). To describe uniformly the bound states and resonant states, we transform the Dirac equation into momentum representation:

$$\int d\vec{k}' \langle \vec{k}|H|\vec{k}'\rangle \psi(\vec{k}') = \varepsilon\psi(\vec{k}), \tag{2}$$

where $\vec{k}$ is wave vector, $H = \vec{\alpha} \cdot \vec{p} + \beta(M + S) + V$ is the Dirac Hamiltonian, and $\psi(\vec{k})$ is the momentum wave function. For a spherical system, $\psi(\vec{k})$ can be separated into the radial and angular parts as

$$\psi(\vec{k}) = \begin{pmatrix} f(k)\phi_{ljm_j}(\Omega_k) \\ g(k)\phi_{\tilde{l}jm_j}(\Omega_k) \end{pmatrix}, \tag{3}$$

where the two-dimensional spinor $\phi_{ljm_j}(\Omega_k) = [\chi_{1/2}(s) \otimes Y_l(\Omega_k)]_{jm_j}$. l ($\tilde{l}$) is the orbital angular momentum corresponding to the large (small) component of Dirac spinor, related to the total angular momentum j with $\tilde{l} = 2j - l$. The treatment of meson fields is the same as that in the case of a neutron. Here, we present the treatment of the Coulomb field. Without losing generality, a screening Coulomb potential is considered:

$$V_c(\vec{r}) = \lambda \frac{\exp(-\eta r)}{r}, \tag{4}$$

where λ represents the strength of Coulomb potential, and η is a screening parameter. With the Coulomb potential, Eq. (1) becomes

$$Mf(k) - kg(k) + \int k'^2 dk' V_c^l(k, k')f(k') = \varepsilon f(k),$$

$$-kf(k) - Mg(k) + \int k'^2 dk' V_c^{\tilde{l}}(k, k')g(k') = \varepsilon g(k), \tag{5}$$

with

$$V_c^l(k, k') = \frac{\lambda}{\pi} \frac{Q_l(y)}{kk'}, \quad V_c^{\tilde{l}}(k, k') = \frac{\lambda}{\pi} \frac{Q_{\tilde{l}}(y)}{kk'}, \tag{6}$$

where $Q_l(y)$ are the Legendre polynomials of the second kind with $y = \frac{k^2 + k'^2 + \eta^2}{2kk'}$. $Q_l(y) = \frac{1}{2}P_l(y)\ln(\frac{y+1}{y-1}) - W_{l-1}(y)$ with $W_{l-1}(y) = \sum_{t=1}^{l} \frac{1}{t}P_{t-1}(y)P_{l-t}(y)$, and $W_{-1}(y) = 0$. $P_l(y)$ is the Legendre polynomial. When $\eta \to 0$ and $k = k'$, there is $y = 1$. There is singularity in $V_c^l(k, k')$ and $V_c^{\tilde{l}}(k, k')$. To eliminate the singularity, Lande subtraction is adopted. The integral in Eq. (5) is separated into the two parts:

$$\int_0^\infty V_c^l(k, k')f_l(k')k'^2 dk' = A + B, \tag{7}$$

where

$$A = \int_0^\infty V_c^l(k, k')\left[f_l(k')k'^2 - \frac{f_l(k)k^2}{P_l(y)}\right]dk', \tag{8}$$

$$B = f_l(k)k^2 \int_0^\infty \frac{V_c^l(k, k')}{P_l(y)}dk'. \tag{9}$$

The integral in A can be set with $k \neq k'$ because $A = 0$ with $k = k'$. The integral in B can be calculated as

$$\int_0^\infty \frac{V_c^l(k, k')}{P_l(y)}dk' = \frac{\lambda}{\pi k}\int_0^\infty \frac{Q_l(y)}{P_l(y)}\frac{dk'}{k'} = \frac{\lambda}{k}\left(\frac{\pi}{2} - I_l\right).$$

I_l can be evaluated exactly, $I_0 = 0$, $I_1 = 1$, $I_2 = 1.224\,744\,871\,391\,589\,4, \ldots$. By using Gauss quadrature for the integral and combining the potentials of exchange mesons, the Dirac Hamiltonian matrix in Eq. (5) is obtained as

$$H = \begin{pmatrix} M\delta_{ab} + \sqrt{w_a w_b}k_a k_b[V_c^l(k_a, k_b) + V_+^l(k_a, k_b)] & -k_a\delta_{ab} \\ -k_a\delta_{ab} & -M\delta_{ab} + \sqrt{w_a w_b}k_a k_b[V_c^{\tilde{l}}(k_a, k_b) + V_-^{\tilde{l}}(k_a, k_b)] \end{pmatrix}, \tag{10}$$

where the on-diagonal matrix elements of the Coulomb potential are given by

$$V_c^l(k_a, k_a) = -\frac{1}{w_a k_a}\frac{\lambda}{\pi}\sum_{b \neq a}\frac{Q_l(y_{ab})w_b}{P_l(y_{ab})k_b} + \frac{1}{w_a k_a}\lambda\left(\frac{\pi}{2} - I_l\right), \tag{11}$$

and the off-diagonal matrix elements are given by

$$V_c^l(k_a, k_b) = \frac{\lambda}{\pi}Q_l(y_{ab})/k_a k_b, \tag{12}$$

with $y_{ab} = \frac{k_a^2 + k_b^2}{2k_a k_b}$. The same expressions hold for $V_c^{\tilde{l}}(k_a, k_b)$ by replacing l with $\tilde{l}$.

For the interaction potentials contributed by exchange mesons, the expressions in momentum representation are the same as those in Ref. [34], i.e.,

$$V_+^l(k_a, k_b) = \frac{2}{\pi}\int r^2 dr[V_o(r) + S(r)]j_l(k_a r)j_l(k_b r),$$

$$V_-^{\tilde{l}}(k_a, k_b) = \frac{2}{\pi}\int r^2 dr[V_o(r) - S(r)]j_{\tilde{l}}(k_a r)j_{\tilde{l}}(k_b r),$$

where $j_l(kr)$ is the spherical Bessel function. In Eq. (10) there are no calculations $Q_l(y_{ab})_{k_a=k_b}$, and the singularity is eliminated. When r is large enough, the Coulomb potential in
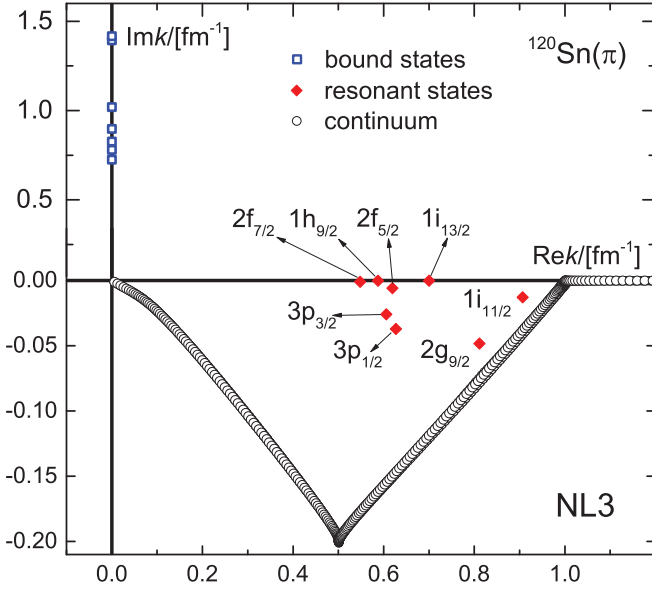
FIG. 1. Single-particle spectra for protons in ^{120}Sn are depicted in the RMF-CMR calculations employing the NL3 parameter set. Bound states, resonant states, and continuum are respectively denoted by blue squares, red diamonds, and black circles.

FIG. 2. The resonant state in ^{37}Sc is illustrated in the upper panel, depicting the complex momentum plane. The lower panel presents the evolution of the energy (in red) and width (in blue) of the $1f_{7/2}$ resonant state towards the imaginary part of the triangular contour vertex. The values for k_r (k_i) are expressed in fm^{-1}, and E (Γ) is denoted in MeV. Note that the values of width should be multiplied by 10^{-3} for proper scaling.

Eq. (4) is exactly the same as that in the RMF calculations. The short-range part is calculated using RMF.

Unlike nonrelativistic programs, the current relativistic formalism, which employs the Lande scheme to address the singularities in the Dirac equation in the momentum representation, necessitates the integration of Coulomb long-range potentials with nuclear short-range potentials. Moreover, it involves multiple self-consistent iterations to solve the coupled Dirac equations for both upper and lower spinors.

III. THE NUMERICAL DETAILS AND RESULTS

In the context of the formalism presented, our investigation focused on single proton resonances within atomic nuclei, using ^{120}Sn as an illustrative example for comparison with other methods. We have performed self-consistent RMF-CMR calculations to analyze single-particle spectroscopy. For neutrons, the Coulomb field is negligible. However, when considering protons, we must incorporate the potential stemming from the exchange mesons with the Coulomb potential. Specifically, for the Coulomb potential, the short-range component is calculated using RMF, while the long-range component is integrated through Eq. (4), setting the strength of the Coulomb field as $\lambda = Ze^2$, where Z represents the electric charge number, and the screening parameter as $\eta = 0.0$. The results, depicted in Fig. 1, reveal distinct separation of bound states, resonant states, and the continuous spectrum, highlighting eight proton resonant states. Notably, resonances $2f_{7/2}$, $1h_{9/2}$, $2f_{5/2}$, and $1i_{13/2}$ are situated near the real k axis, indicating narrow resonance, while resonances $3p_{1/2}$, $3p_{3/2}$, $1i_{11/2}$, and $2g_{9/2}$ are positioned farther from the real k axis, representing broad resonance. It is noteworthy that resonances $i_{11/2}$ and $2g_{9/2}$, not obtained in RMF-CSM calculations due to divergence caused by a large complex rotation potential, are successfully captured by the RMF-CMR method. This
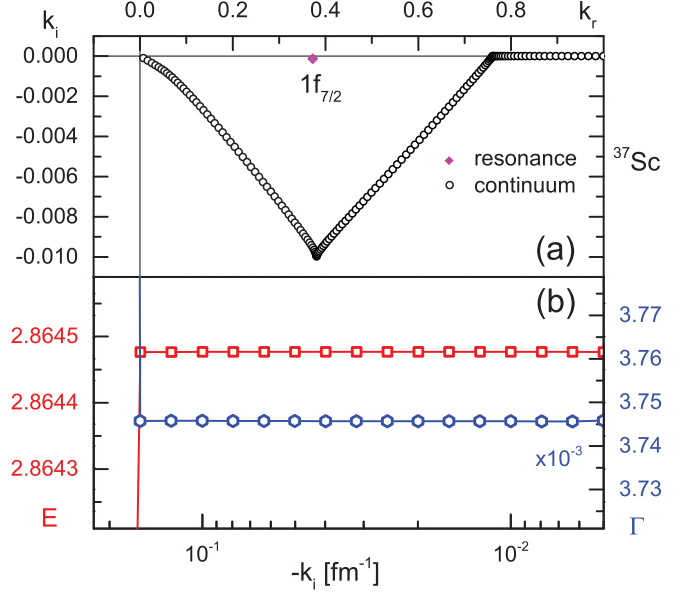
underscores the power and efficiency of the RMF-CMR approach in exploring broad resonances, provided the momentum contour encompasses the resonance range. Other existing methods also face challenges in addressing these resonances, highlighting the unique efficacy of the RMF-CMR method in such investigations.

To showcase the merits of our calculations, a comprehensive comparison is conducted with alternative methods, including RMF-S [22], RMF-ACCC [17], RMF-CSM [19], and RMF-GF [21]. The results, summarized in Table I, show comparability in calculated energies and widths across all the eight resonant states with alternative methods. Notably, the RMF-CMR calculation demonstrates closer agreement with the RMF-S approach, recognized for its accuracy as a scattering method. This suggests that RMF-CMR serves as a more precise method, akin to bound-state approaches, for characterizing resonant states.

Given the efficacy of the recently developed RMF-CMR method in exploring single proton resonances, we employ this approach to investigate single proton emission. To ensure a meaningful comparison, we select ^{37}Sc and ^{39}Sc as illustrative examples, utilizing identical scalar and vector potentials as those employed in Ref. [44]. In Fig. 2(a) the results for ^{37}Sc are presented, clearly revealing the $1f_{7/2}$ single proton resonance in the complex momentum plane. To accurately determine resonance parameters, it is imperative to examine the dependence of the calculated results on the integration contour. Figure 2(b) displays the energy and width variations with respect to the imaginary part of the triangular contour vertex. As $-k_i$ decreases from 0.1 to 0.01 or lower, both the calculated resonance energy and width exhibit minimal

TABLE I. The energies and widths of single proton resonant states in ^{120}Sn, as calculated using the RMF-CMR method, are presented alongside comparisons with other computational approaches. In this analysis the NL3 parameter set is employed, and all energy values are expressed in MeV.

	$2f_{7/2}$ E, Γ	$1h_{9/2}$ E, Γ	$3p_{3/2}$ E, Γ	$2f_{5/2}$ E, Γ
RMF-CMR	6.210, 0.042	7.133, 0.003	7.567, 1.291	7.917, 0.294
RMF-S	6.210, 0.043	7.132, 0.003	7.513, 0.924	7.934, 0.307
RMF-GF	6.205, 0.037	7.134, 0.002	7.265, 0.965	7.909, 0.365
RMF-ACCC	6.220, 0.073	7.130, 0.017	7.320, 0.820	7.970, 0.300
RMF-CSM	6.207, 0.048	7.135, 0.003	7.305, 0.911	7.919, 0.282
	$3p_{1/2}$ E, Γ	$1i_{13/2}$ E, Γ	$2g_{9/2}$ E, Γ	$1i_{11/2}$ E, Γ
RMF-CMR	8.166, 2.052	10.110, 0.012	13.510, 3.208	16.889, 0.946
RMF-S	8.085, 1.344	10.110, 0.012		16.960, 0.999
RMF-GF	7.667, 1.233	10.110, 0.014		16.934, 1.092
RMF-ACCC	7.690, 1.130			
RMF-CSM	7.663, 1.222			

changes. The resonance energy remains nearly constant for the first five significant digits, while the width remains essentially unchanged for the first three significant digits, ensuring the necessary numerical accuracy. A similar contour-independent determination of resonance parameters is obtained for ^{39}Sc. The obtained energy and width values for ^{39}Sc are listed in Table II. Additionally, results from time-dependent Dirac (TD-Dirac), CSM, and SM methods are included for comparison, and the experimental data source is from Refs. [45,46].

In the case of single proton emission in ^{37}Sc, the Q values calculated by the four methods exhibit remarkable consistency and align closely with experimental data. Our calculations closely match the results obtained from TD-Dirac calculations. Similarly, the width values calculated by all four methods show substantial agreement, with our calculations demonstrating better alignment with TD-Dirac

TABLE II. The Q value and width (lifetime) of $1p$ emission assessed in the $f_{7/2}$ channel using the present method are compared with results obtained from other methods. Q and Γ are given in MeV, while τ is expressed in seconds.

^{37}Sc $= {}^{36}$Ca $+ p$		
Method	Q	$\Gamma (\tau)$
CMR	2.864	3.75×10^{-3} (1.75×10^{-19})
TD-Dirac	2.864	3.74×10^{-3} (1.76×10^{-19})
CSM	2.863	3.82×10^{-3} (1.72×10^{-19})
SM	2.863	3.62×10^{-3} (1.82×10^{-19})
Experiment	2.9(3)	–
^{39}Sc $= {}^{38}$Ca $+ p$		
Method	Q	$\Gamma (\tau)$
CMR	0.664	3.88×10^{-9} (1.69×10^{-13})
TD-Dirac	0.662	3.87×10^{-9} (1.70×10^{-13})
Experiment	0.597(24)	($\tau < 400$ ns)

results. Turning to single proton emission in ^{39}Sc, our calculations successfully reproduce the experimental Q value, displaying consistency with TD-Dirac calculations. In contrast, the other two bound-state-like methods achieve consistent Q values but encounter challenges in achieving similarly small width values. It is crucial to acknowledge that describing extraordinarily narrow resonances poses a significant challenge, and determining their widths across various methods, especially those relying on bound states, presents additional complexities. The present method exhibits a notable capability to explore extremely narrow resonances, surpassing other bound-state-like methods in this particular aspect.

Furthermore, we applied the RMF-CMR method to study proton-rich exotic nuclei, using ^{26}P as an illustrative example and comparing it with the RMF method. We considered box radii of $R_c = 10$, 15, and 20 fm. The proton density distributions obtained are depicted in Fig. 3. In the RMF calculations, the proton density distributions were noticeably influenced by the box size, exhibiting a sharp drop near the box's edge. However, in the RMF-CMR calculations, proton density distributions decayed uniformly with increasing radius, irrespective of the box size. This uniform decay is attributed to the fact that the RMF-CMR calculation was performed in momentum space, eliminating any dependency on the box size in coordinate space. Our results highlight the capability of the RMF-CMR method to provide a reliable description of proton density distribution in exotic nuclei, a crucial aspect for understanding their structure and properties. Additionally, our observations revealed that the proton density distribution was more extended compared to the neutron density distribution, indicative of the presence of a proton halo. This finding is consistent with experimental observations [47,48].

To understand the physical mechanism responsible for the proton halo in ^{26}P, it is essential to analyze the density distributions of individual particle levels, as illustrated in Fig. 4. The $1s_{1/2}$ level, being deeply bound, displays the most orderly and least diffuse density distribution. Conversely, the $1p_{3/2}$, $1p_{1/2}$, and $1d_{5/2}$ levels, with lesser binding energies,
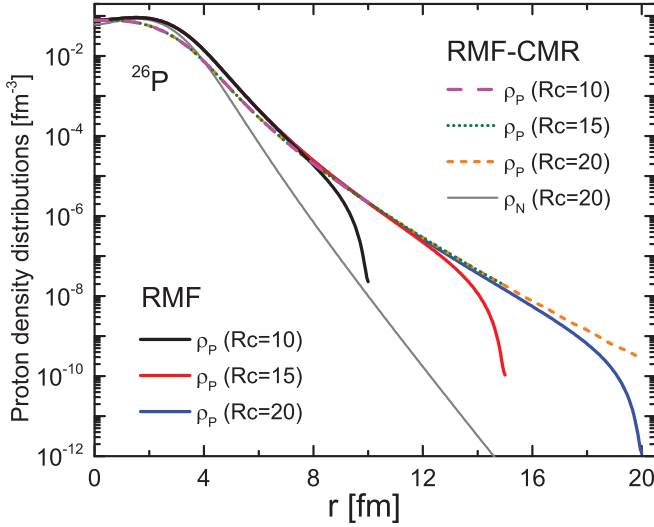
FIG. 3. Proton density distributions in ^{26}P for various R_c values are depicted in the figure, with solid lines representing results from the RMF calculations, and dashed lines from the RMF-CMR calculations. Additionally, for comparison, the neutron density distributions obtained from the RMF-CMR calculations are illustrated by the gray line. The box radius R_c is given in femtometers (fm).
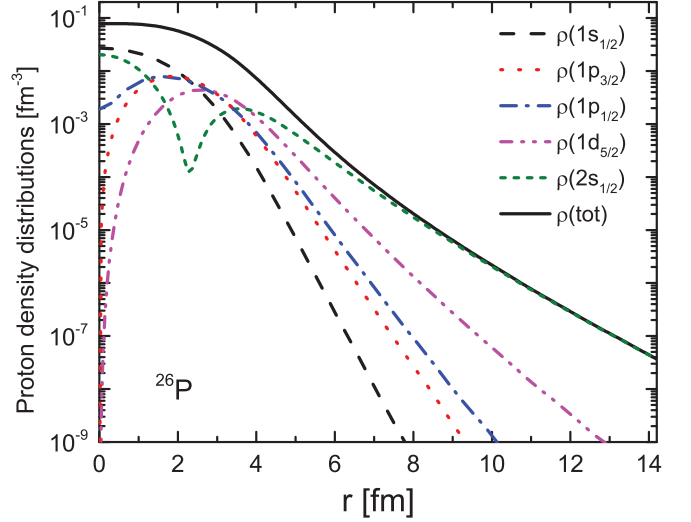

FIG. 4. The density distributions represent the occupied single-particle levels for protons, encompassing $1s_{1/2}$, $1p_{3/2}$, $1p_{1/2}$, $1d_{5/2}$, and $2s_{1/2}$. Additionally, for comparative analysis, the overall density distribution of protons is also depicted.

exhibit somewhat more diffuse density distributions. The $2s_{1/2}$ level, residing near the Fermi surface and being the least bound, demonstrates a significantly diffuse density distribution. Notably, the last valence proton in ^{26}P occupies this level. Beyond $r > 8$ fm, the total proton density distribution precisely aligns with that of the $2s_{1/2}$ level. This observation implies that the proton halo in ^{26}P is predominantly defined by the protons occupying the $2s_{1/2}$ level, and the important role of the $2s_{1/2}$ orbital in the predicted halo structure of the neutron-deficient phosphorus isotopes has been confirmed experimentally [47].

IV. SUMMARY

We have introduced an enhanced relativistic density functional theory that comprehensively addresses proton resonances, emission processes, and proton-rich exotic nuclei. The theory effectively resolves the long-range Coulomb potential issue by eliminating its singularity in the Dirac equation through the complex momentum representation. When applying this theoretical framework to study proton resonances in ^{120}Sn, it shows remarkable improvements over traditional methods, particularly in capturing the nuances of narrow and broad resonances. Comparisons with alternative

techniques, including RMF-S, RMF-ACCC, RMF-CSM, and RMF-GF, underscore the precision of our newly introduced RMF-CMR method in characterizing resonant states. Our investigation further extends to single proton emission from ^{37}Sc and ^{39}Sc, where the method reproduces experimental Q values and lifetimes with exceptional accuracy, particularly for extremely narrow resonances. The application of the RMF-CMR method to proton-rich exotic nuclei, such as ^{26}P, reveals uniform proton density distributions that are unaffected by box size constraints, unlike traditional RMF calculations. Our method aptly describes the proton halo in ^{26}P, attributing its presence to protons occupying the weakly bound $2s_{1/2}$ level. This study offers insights into nuclear phenomena in proton-rich systems, providing a more reliable understanding of their structure and properties that were previously difficult to unravel.

[1] A. Bonaccorso, Prog. Part. Nucl. Phys. **101**, 1 (2018).

[2] M. Pfützner, I. Mukha, and S. M. Wang, Prog. Part. Nucl. Phys. **132**, 104050 (2023).

[3] I. Tanihata, H. Savajols, and R. Kanungo, Prog. Part. Nucl. Phys. **68**, 215 (2013).

[4] T. Nakamura, H. Sakurai, and H. Watanabe, Prog. Part. Nucl. Phys. **97**, 53 (2017).

[5] R. J. Liotta, E. Maglione, N. Sandulescu, and T. Vertse, Phys. Lett. B **367**, 1 (1996).

[6] N. Michel, W. Nazarewicz, M. Ploszajczak, and K. Bennaceur, Phys. Rev. Lett. **89**, 042502 (2002).

[7] M. Matsuo, Nucl. Phys. A **696**, 371 (2001).

[8] H. Oba and M. Matsuo, Phys. Rev. C **80**, 024301 (2009).

[9] Y. Zhang, M. Matsuo, and J. Meng, Phys. Rev. C **86**, 054318 (2012).

[10] D. Vretenar, A. V. Afanasjev, G. A. Lalazissis, and P. Ring, Phys. Rep. **409**, 101 (2005).

[11] J. Meng, H. Toki, S. G. Zhou, S. Q. Zhang, W. H. Long, and L. S. Geng, Prog. Part. Nucl. Phys. **57**, 470 (2006).

[12] T. Nikšić, D. Vretenar, and P. Ring, Prog. Part. Nucl. Phys. **66**, 519 (2011).

[13] H. Z. Liang, J. Meng, and S. G. Zhou, Phys. Rep. **570**, 1 (2015).

[14] X. D. Xu, B. Sun, Z. M. Niu, Z. Li, Y.-Z. Qian, and J. Meng, Phys. Rev. C **87**, 015805 (2013).

[15] Z. M. Niu, Y. F. Niu, H. Z. Liang, W. H. Long, T. Nikšić, D. Vretenar, and J. Meng, Phys. Lett. B **723**, 172 (2013).

[16] H. Shen, F. Ji, J. Hu, and K. Sumiyoshi, Astrophys. J. **891**, 148 (2020).

[17] S. S. Zhang, J. Meng, S. G. Zhou, and G. C. Hillhouse, Phys. Rev. C **70**, 034308 (2004).

[18] L. Zhang, S. G. Zhou, J. Meng, and E. G. Zhao, Phys. Rev. C **77**, 014312 (2008).

[19] J. Y. Guo, X. Z. Fang, P. Jiao, J. Wang, and B. M. Yao, Phys. Rev. C **82**, 034318 (2010).

[20] M. Shi, Q. Liu, Z. M. Niu, and J. Y. Guo, Phys. Rev. C **90**, 034319 (2014).

[21] T. T. Sun, S. Q. Zhang, Y. Zhang, J. N. Hu, and J. Meng, Phys. Rev. C **90**, 054321 (2014).

[22] N. Sandulescu, L. S. Geng, H. Toki, and G. C. Hillhouse, Phys. Rev. C **68**, 054323 (2003).

[23] Z. P. Li, J. Meng, Y. Zhang, S.-G. Zhou, and L. N. Savushkin, Phys. Rev. C **81**, 034311 (2010).

[24] B.-N. Lu, E.-G. Zhao, and S.-G. Zhou, Phys. Rev. Lett. **109**, 072501 (2012).

[25] B.-N. Lu, E.-G. Zhao, and S.-G. Zhou, Phys. Rev. C **88**, 024323 (2013).

[26] M. Shi, J.-Y. Guo, Q. Liu, Z.-M. Niu, and T.-H. Heng, Phys. Rev. C **92**, 054313 (2015).

[27] M. Shi, X.-X. Shi, Z.-M. Niu, T. T. Sun, and J.-Y. Guo, Eur. Phys. J. A **53**, 40 (2017).

[28] C. V. Sukumar, J. Phys. A **12**, 1715 (1979).

[29] Y. R. Kwon and F. Tabakin, Phys. Rev. C **18**, 932 (1978).

[30] T. Berggren, Nucl. Phys. A **109**, 265 (1968).

[31] G. Hagen and J. S. Vaagen, Phys. Rev. C **73**, 034321 (2006).

[32] A. Deltuva, Few-Body Syst. **56**, 897 (2015).

[33] N. Michel and M. Ploszajczak, *Gamow Shell Model, The Unified Theory of Nuclear Structure and Reactions*, Lecture Notes in Physics Vol. 983 (Springer, New York, 2022).

[34] N. Li, M. Shi, J. Y. Guo, Z. M. Niu, and H. Z. Liang, Phys. Rev. Lett. **117**, 062502 (2016).

[35] K. M. Ding, M. Shi, J. Y. Guo, Z. M. Niu, and H. Z. Liang, Phys. Rev. C **98**, 014316 (2018).

[36] X. N. Cao, Q. Liu, Z. M. Niu, and J. Y. Guo, Phys. Rev. C **99**, 024314 (2019).

[37] Z. Fang, M. Shi, J. Y. Guo, Z. M. Niu, H. Liang, and S. S. Zhang, Phys. Rev. C **95**, 024311 (2017).

[38] X. W. Wang and J. Y. Guo, Phys. Rev. C **104**, 044315 (2021).

[39] Y.-X. Luo, Q. Liu, and J.-Y. Guo, Phys. Rev. C **108**, 024320 (2023).

[40] K. M. Maung, D. E. Kahana, and J. W. Norbury, Phys. Rev. D **47**, 1182 (1993).

[41] J. W. Norbury, K. M. Maung, and D. E. Kahana, Phys. Rev. A **50**, 2075 (1994).

[42] N. Michel, Phys. Rev. C **83**, 034325 (2011).

[43] G. Hagen and N. Michel, Phys. Rev. C **86**, 021602(R) (2012).

[44] T. Oishi, Phys. Rev. C **107**, 034301 (2023).

[45] National Nuclear Data Center, Chart of Nuclides in NUDAT 3.0, https://www.nndc.bnl.gov/nudat3/.

[46] M. Wang, W. Huang, F. Kondev, G. Audi, and S. Naimi, Chin. Phys. C **45**, 030003 (2021).

[47] A. Navin, D. Bazin, B. A. Brown, B. Davids, G. Gervais, T. Glasmacher, K. Govaert, P. G. Hansen, M. Hellstrom, R. W. Ibbotson, V. Maddalena, B. Pritychenko, H. Scheit, B. M. Sherrill, M. Steiner, J. A. Tostevin, and J. Yurkon, Phys. Rev. Lett. **81**, 5089 (1998).

[48] D. Pérez-Loureiro, C. Wrede, M. B. Bennett, S. N. Liddick, A. Bowe, B. A. Brown, A. A. Chen, K. A. Chipps, N. Cooper, D. Irvine, E. McNeice, F. Montes, F. Naqvi, R. Ortez, S. D. Pain, J. Pereira, C. J. Prokop, J. Quaglia, S. J. Quinn, J. Sakstrup *et al.*, Phys. Rev. C **93**, 064320 (2016).